Nano Research Energy

ISSN 2791-0091 (print); 2790-8119 (online)
https://doi.org/10.26599/NRE.2025.9120187

Research Article

Flexible and self-powered paper-based artificial synapse for neuromorphic computing and 3d information transmission

Nuo Xu[1,2], Yifei Wang[2], Ziwei Huo[2,3], Jinran Yu[2], Jiahong Yang[1,3], Zhong Lin Wang[2,4] (✉), and Qijun Sun[1,2,3,5] (✉)

[1] *Center on Nanoenergy Research, School of Physical Science and Technology, Guangxi University, Nanning 530004, China*
[2] *Beijing Institute of Nanoenergy and Nanosystems, Chinese Academy of Sciences, Beijing 101400, China*
[3] *School of Nanoscience and Technology, University of Chinese Academy of Sciences, Beijing 100049, China*
[4] *Georgia Institute of Technology, Atlanta GA 30332, USA*
[5] *Shandong Zhongke Naneng Energy Technology Co., Ltd., Dongying 257061, China*

Received: 29 April 2025 / **Revised:** 7 July 2025 / **Accepted:** 14 July 2025 / **Published date:** 9 September 2025

ABSTRACT

The advent of the Internet of Things (IoT) era has significantly accelerated advancements in neuromorphic computing research. Triboelectric nanogenerators (TENGs) exhibit dual functionality as both energy harvesters and synaptic simulators, facilitated by their inherent mechanoelectrical transduction properties and seamless circuit integration capabilities. In this work, we presented a vertically contact-separated paper-based artificial synaptic device employing TENG technology. The fabricated device successfully replicates fundamental synaptic behaviors, including paired-pulse facilitation (PPF), high-pass filtering characteristics, and spatiotemporal dynamic logic operations. Through optimized circuit configurations, we achieved elementary "NOT" logic gate using single devices, while implementing "AND/NAND" logic gates and "OR/NOR" logic gates operations through two- and three-device assemblies, respectively. Capitalizing on the mechanical flexibility and lightweight of paper substrates, we further developed a trilayer artificial synaptic architecture that mimics hierarchical neural information processing. This mechanoelectrical coupling approach establishes a novel paradigm for flexible neuromorphic systems, demonstrating exceptional potential for environmentally interactive robotics and adaptive wearable prosthetics.

KEYWORDS

artificial synapse, triboelectric nanogenerators, self-powered, paper-based, neuromorphic device, logic gate

1 Introduction

The neural network of the brain, as the core carrier of biological intelligence, derives its unique advantages from two key characteristics: parallel computing architecture and synaptic plasticity mechanisms. The three-dimensional (3D) network formed by 86 billion neurons through synaptic connections possesses trillions of parallel pathways, enabling multimodal information integration and nonlinear computation (arising from neuronal threshold activation and neurotransmitter modulation) [1–5]. This architecture allows the brain to simultaneously process environmental information in real-time while dynamically optimizing information storage strategies. The brain's remarkable capabilities fundamentally stem from its neural network composed of neurons and synapses [6, 7]. Synapses, serving as communication channels between neurons, exhibit their most prominent feature—synaptic plasticity. As the material basis of neural computability, synaptic plasticity manifests as adaptive changes in synaptic efficacy depending on neural activity patterns. The Hebbian principle of "cells that fire together wire together" is molecularly embodied through bidirectional regulation mechanisms: long-term potentiation/depression [8–15]. This synaptic weight adjustment mechanism not only underlies memory formation (as exemplified by cognitive map construction through place cells in the hippocampal region) but also endows neural networks with continuous learning capacity.

Biological studies reveal that simulating brain functions necessitates the successful fabrication of physical devices emulating biological synaptic capabilities [16, 17]. Current synaptic devices predominantly adopt either simple two-terminal memristors or three-terminal transistors [6, 18–22]. With the accelerated advancement of the Internet of Everything era, the number of Internet of Things (IoT) nodes is projected to exceed 100 billion by 2030, imposing two critical requirements on computing systems: ultrahigh-throughput data processing capability (> 10^{15} operations/s) and ultralow-power operation (< 1 μW/device). Synaptic devices, as a novel class of electronic components, demonstrate significant potential to revolutionize conventional data storage and computational paradigms.

Address correspondence to Zhong Lin Wang, zhong.wang@mse.gatech.edu; Qijun Sun, sunqijun@binn.cas.cn

Specifically, memristive devices and synaptic transistors enable neuromorphic computation that emulates human brain functionality, thereby achieving high-performance parallel processing capabilities that circumvent the von Neumann bottleneck [23]. Representative examples include electric-double-layer transistors, optoelectronic transistors, ferroelectric memristors, and the recently developed sodium lignosulfonate-intercalated memristors, all of which exhibit remarkable performance in neuromorphic computing applications [24–27]. Current silicon-based electronic devices relying on von Neumann architecture face inherent limitations due to rigid substrates and physical scaling boundaries (e.g., quantum tunneling effects at 5 nm process nodes), rendering them inadequate to meet the stringent demands of distributed intelligent nodes for mechanical flexibility, environmental adaptability, and sustainability [28–33]. Emerging triboelectric nanogenerators (TENGs) technology—traditionally used for energy harvesting—exhibit significant potential in neuromorphic device development due to advantages, such as self-powering capacity, broad material compatibility, and simplified fabrication processes [34–36]. Combining TENG and paper-based materials (one of Earth's most abundant renewable resources), it may offer an energy-autonomy and self-sufficient platform for versatile neuromorphic applications with multifunctionality due to the hierarchically porous structure and surface chemical modifiability of paper-based materials [37–42]. In terms of device architecture innovation, paper-based electronics demonstrate exceptional mechanical robustness, ecological compatibility, and manufacturing cost-effectiveness. Leveraging their unique material–property coupling effects, paper-based neuromorphic devices exhibit immense potential for future artificial intelligence applications [43–48].

Herein, we designed a paper-based artificial synaptic device employing a vertically contact–separation mode TENG. Despite its structural simplicity, this device successfully emulates synaptic characteristics due to the similarity between its equivalent circuit diagram and that of neuronal models. The paper-based synaptic device demonstrates short-term plasticity (STP) behaviors, including paired-pulse facilitation (PPF), high-pass filtering, and spatiotemporal dynamic logic. Beyond fundamental synaptic emulation, we expanded its computational capabilities by constructing a reconfigurable logic gate array based on the nonlinear superposition principle of synaptic weights. To address complex information processing demands, a three-dimensional vertically integrated architecture was developed through modulation of displacement stimulus intensity (d), enabling information recognition and transmission in a three-layer array of paper-based artificial synapses.

2 Results and discussion

2.1 The principle of paper-based artificial synapses

The paper-based artificial synaptic device we developed achieves multi-dimensional biomimetic reconstruction of biological neural systems. Its operational principles exhibit deep topological isomorphism with biological neurons in terms of ion transport, membrane potential modulation, and signal integration [5, 17]. In biological neurons, the lipid bilayer of the cell membrane acts as an insulating barrier, separating the highly conductive intracellular cytoplasm from the extracellular fluid (Fig. 1(a)). Strictly speaking, the cell membrane functions as a leaky capacitor (C_m), as ion channels penetrate the membrane under external stimuli [49]. Analogous to how a capacitor stores and releases charge via current flow, the equivalent circuit model provides an intuitive framework to quantitatively describe how ionic movement generates electrical signals in neurons, bridging the discrete physical properties of the membrane with its electrical characteristics.

The leaky integrate-and-fire (LIF) neuron model provides a highly effective framework for describing the behavior of membrane potential. As shown in Fig. 1(b), the core components of the equivalent circuit exhibit precise correspondence with biological structures: (1) conductor or resistor (R), representing ion channels, simulates the ionic permeability of the lipid membrane at rest; (2) voltage source (V_{rest}), representing the ionic concentration gradient; (3) capacitor (C), representing the charge storage capacity of the cell membrane; and (4) current source (I_{inj}), representing external stimuli, which mimics the spatiotemporal modulation of presynaptic action potentials [50, 51]. In the absence of input, the membrane potential remains at the resting value V_{rest}

$$I(t) = I_R + I_c = \frac{V(t) - V_{rest}}{R} + C\frac{dV(t)}{dt} \quad (1)$$

where $I(t)$ is the total input current across the membrane at a certain moment (t), I_R is the current flowing through the resistor, I_c is the current flowing through the capacitor, and $V(t)$ is the membrane potential difference at a certain moment.

By solving the differential equation, it can be obtained

$$V(t) = V_{rest} + (V_0 - V_{rest})\exp\left(-\frac{t - t_0}{\tau'}\right) \quad (2)$$

where V_0 and t_0 are the initial conditions and $\tau' = RC$ is the membrane time constant of the neuron, which shows that the LIF neuron model is exponential. When the presynaptic membrane receives a pulsatile stimulus, an exponential signal is generated in the postsynaptic membrane.

The paper-based artificial synaptic devices developed in this study successfully replicate this intricate biological mechanism (Fig. 1(c)). Upon application of mechanical stimuli (e.g., tactile or pressure inputs), these external forces are transduced into electrical signals that closely resemble biological excitatory postsynaptic potentials (EPSPs). As shown in Fig. 1(d), the TENG fundamentally operates as a capacitor, where its output voltage corresponds to the potential difference measured between its two electrodes [36, 51–53]. This voltage comprises two components: (1) intrinsic capacitance (C') between the TENG's two electrodes, representing their inherent charge storage capability and (2) ideal voltage source (V_{OC}), which characterizes the TENG's open-circuit voltage arising from triboelectric charges during contact–separation and electrostatic induction. When the contact–separation mode TENG operates with a connected R, opposite triboelectric charges with equal surface charge density are generated at the contact interface between the top electrode and the dielectric layer due to contact electrification [54–58]. As the two triboelectric layers begin to separate, the surface charge density on the electrodes evolve with increasing separation distance (x) due to electrostatic induction. The actual charge transfer rate is constrained by the external R according to Ohm's law, and the output voltage can be expressed as

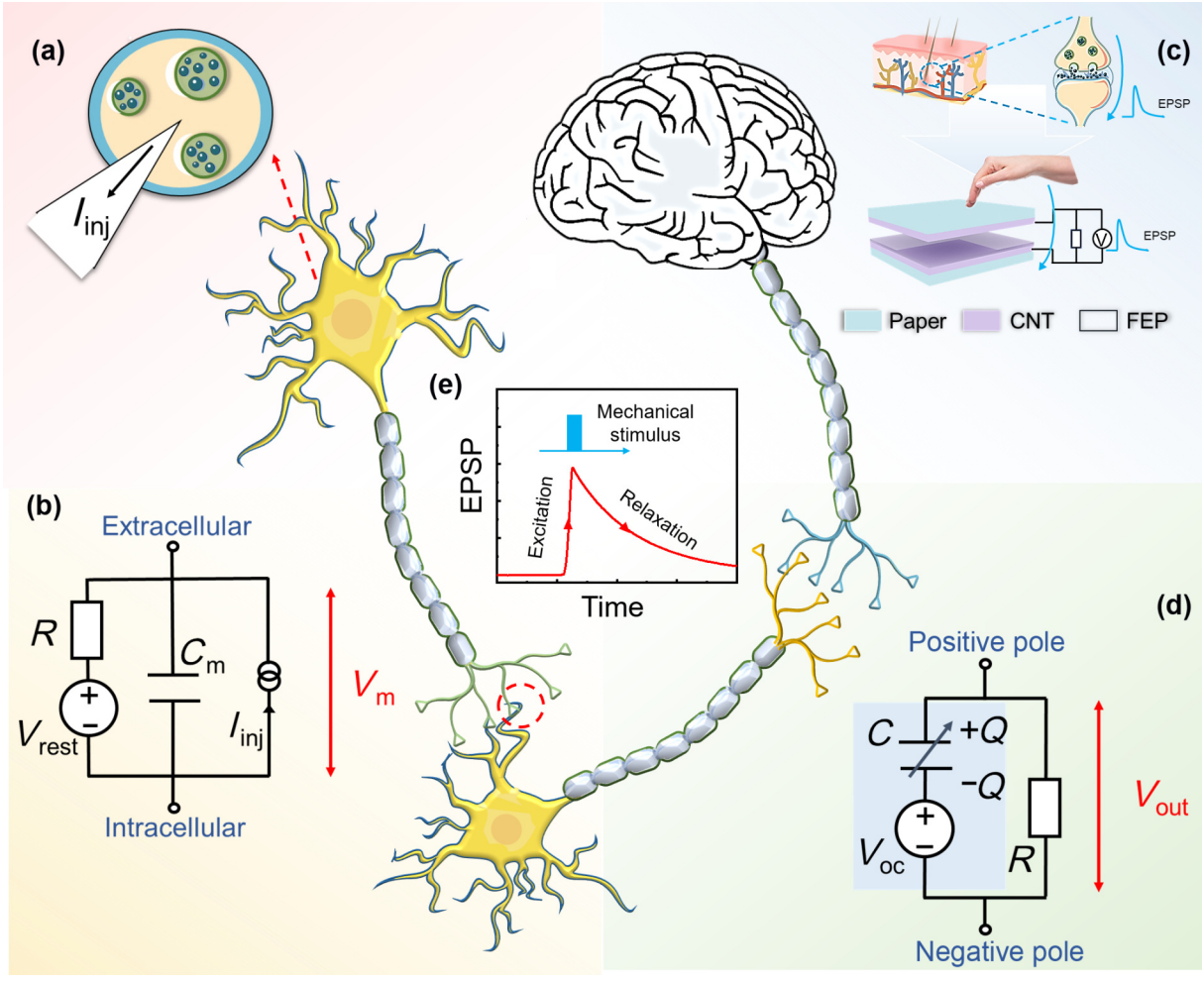

Figure 1 Paper-based artificial synapse corresponding to the biological nerve system. (a) Schematic diagram of the neuronal cell. (b) Equivalent circuit diagram of the neuronal cell. (c) Schematic diagram of the paper-based artificial synapse. (d) Equivalent circuit diagram of the paper-based artificial synapse. (e) EPSP induced by TENG.

$$V(t) = R \cdot I(t) = R\frac{\mathrm{d}Q}{\mathrm{d}t} = \frac{\sigma x(t)}{\varepsilon_0} - \frac{d' + x(t)}{S\varepsilon_0} \times e^{-\int_0^t \frac{d'+x(\tau)}{RS\varepsilon_0}\mathrm{d}\tau} \times \int_0^t \frac{\sigma x(\tau)}{R\varepsilon_0} e^{-\int_0^\tau \frac{d'+x(z)}{RS\varepsilon_0}\mathrm{d}z}\mathrm{d}\tau \quad (3)$$

in this equation, Q is the transferred charge, S is the contact area, ε_0 is the air dielectric constant, d' is the effective thickness, σ is the surface charge density of the dielectric, $x(t)$ is the pole–plate spacing, and τ is correlated with the load resistance and the intrinsic capacitance of the TENG.

The TENG exhibits an equivalent circuit structure that closely resembles that of leaky LIF neurons, demonstrating analogous excitation (charging) and relaxation (discharging) processes. Notably, the relaxation phase follows an exponential decay pattern governed by the system resistance. While LIF neurons represent a simplified engineering model employing constant current inputs, biological systems typically exhibit more complex behavior. In contrast, TENGs can emerge as promising artificial synaptic devices, offering tunable synaptic weights through resistance modulation and contact–separation distance adjustment. Figure 1(e) presents the characteristic EPSP output profile of the TENG device. Upon mechanical stimulation under load resistance conditions, the device reliably reproduces the fundamental synaptic processes of excitation and relaxation.

To elucidate the operational mechanism of TENG devices under load resistance conditions, we conducted systematic investigations. Figure S1 in the Electronic Supplementary Material (ESM) illustrates the fundamental working principle: When an external force separates the two triboelectric layers, contact electrification induces the generation of equal but opposite surface charges at the interface. According to the capacitor model, this separation results in a gradual voltage increase across the device, corresponding to the charging process (Fig. S1(ii) in the ESM). Subsequently, the device discharges through the load resistor, exhibiting a characteristic exponential voltage decay as charges dissipate (Figs. S1(iii)(1)–S1(iii)(3) in the ESM). The discharge rate exhibits an inverse relationship with the load resistance value, mirroring the EPSP decay dynamics observed in biological synapses during neurotransmitter diffusion. This time-dependent response profile provides the physical foundation for implementing synaptic plasticity mechanisms, including short-term potentiation. Upon re-approximation of the triboelectric layers, the interelectrode distance decreases, increasing capacitance and inducing reverse current flow. Contact between the layers generates a maximum negative potential difference (Fig. S1(iv) in the ESM), initiating a new charging cycle, followed by subsequent discharge through the load resistor (Figs. S1(i)(1)–S1(i)(3) in the ESM).

The material characterization of the paper-based artificial synaptic device was systematically performed using scanning

electron microscopy (SEM), as presented in Fig. S2 in the ESM. Comparative analysis reveals distinct surface morphological differences among three key regions: pristine Teslin paper, Teslin–carbon nanotube (CNT) composite, and Teslin–CNT–fluorinated ethylene propylene (FEP) multilayer structures. SEM imaging clearly demonstrates the successful deposition of CNTs on Teslin substrates, with FEP overlayers exhibiting characteristic height variations (Fig. S2 in the ESM). Cross-sectional analysis (Figs. S3 and S4 in the ESM) further elucidates the device architecture. In the Teslin–CNT–FEP composite (Figs. S3(a) and S3(b) in the ESM), CNTs remain obscured due to the structural continuity between the FEP film and Teslin substrate in the intermediate region. Quantitative evaluation of the CNT layer thickness was conducted using Teslin–CNT cross-sections (Fig. S3(c) in the ESM), revealing a homogeneous distribution (35.3 μm) with occasional paper-derived particulates (Fig. S3(d) in the ESM). High-magnification imaging (Figs. S3(e) and S3(f) in the ESM) confirms the coexistence of CNT networks and Teslin matrix. Complementary measurements indicate an FEP layer thickness of 0.05 mm (Fig. S4 in the ESM). This optimized CNT thickness achieves an optimal balance between electrical conductivity and mechanical flexibility, fulfilling the operational requirements of synaptic devices.

2.2 Characterization of typical synaptic properties of paper-based artificial synapse device

The synapse is a specialized cellular connection between neuronal cells or between neuronal and non-neuronal cells, and it is a key structure for the exchange of information and physiological activities between neurons [36, 59]. The structural and functional integrity of synapses is essential to ensure that neurons receive information and successfully transmit, process, and store it. The synapse is composed of three parts: the presynaptic membrane, the synaptic gap, and the postsynaptic membrane. The presynaptic membrane is the nerve endings of the previous neuron, and the postsynaptic membrane is the cell body of the next neuron or the dendrites surrounding it. The active area of the presynaptic membrane contains a large number of synaptic vesicles, which contain chemicals called neurotransmitters [5, 60, 61]. When the presynaptic membrane is stimulated by an excitatory afferent stimulus, the released neurotransmitter reaches the postsynaptic membrane through the synaptic gap and binds to receptors in the postsynaptic membrane, causing a transient depolarization that results in an EPSP.

The effectiveness of a synapse is measured by the establishment of connections between pre- and postsynaptic neurons, called synaptic weight (or synaptic strength), which can be precisely adjusted by the concentration of ionic substances (e.g., Ca^{2+}, Na^{+}, and K^{+}). The successful preparation of physical devices with synaptic functions is important for the hardware implementation of neuromorphic computing systems. Similar to biological synapses, the output voltage of paper-based artificial synapses can be precisely tuned by adjusting the value of the series resistance [62]. Applying a displacement stimulus to one side of the paper-based synapse at a certain distance induces a transient output voltage, and such a nonlinear output voltage is very similar to the EPSP in biological synapses. The resistance value of the series resistor can be regarded as the synaptic weight. Figure 2(a) shows a schematic diagram of our paper-based artificial synaptic device compared with biological synapses.

The typical EPSP behavior of the paper-based artificial synapse is characterized in Fig. 2(b). A 5 GΩ resistor is connected in series in a paper-based TENG device to which a displacement stimulus is applied. The displacement stimulus acts as a presynaptic input to charge the friction layer, and then the resistor induces charge movement and triggers the EPSP. When the input displacement is 2 mm, the EPSP is 14.49 V. During the contact of the device, the EPSP gradually decays to its initial value (Fig. 2(b)). The decay time (τ) of the device under this condition was estimated to be ~ 10 s by an exponential decay model fitting, indicating a characteristic time of ~ 10 s for charge migration (Fig. 2(c)). In addition to this, we also investigated the effects of different displacement stimuli, different device sizes, and different resistance values on EPSP, which are shown in Figs. S5(a)–S5(c) in the ESM, respectively. The comparison shows that all three parameters have a positive gain on EPSP, with a single displacement stimulus having a smaller effect on EPSP. The device size has a greater effect on EPSP, which may be due to the increasing surface charges with increasing area. The resistance value not only affects the EPSP but also has a significant effect on the decay time, which may be attributed to the fact that the resistance value closely determines the charge transfer process. We fitted the decay for different resistance conditions to obtain a linear increment in τ with increasing resistance value (inset in Fig. 2(c)).

Since the nervous system receives an endless amount of information from the outside world, it is essential to extract useful information from this huge amount of information. In the nervous system, short-range synaptic plasticity (e.g., STP) in biological synapses is regarded as the key to information extraction [5, 7, 59, 60]. STP is mostly triggered by short bursts of activity, where a short interval between two input stimuli causes a temporary accumulation of Ca^{2+} in the presynaptic membrane. This leads to changes in the physiological processes that modulate synaptic vesicle cytokinesis and ultimately the release of neurotransmitters. STP generally lasts from milliseconds to minutes and is often important for short-range adaptation, short-range altered behavior, and short-range memory of inputs. Therefore, STP plays an important role in synaptic computation and information processing. The change in synaptic strength evoked by two paired-pulse stimulations of equal intensity and millisecond interval is a typical STP behavior. The direction and magnitude of synaptic strength change are usually expressed by the paired-pulse ratio (PPR), which is the ratio of the amplitude of synaptic strength triggered by stimulus 2 to that of stimulus 1, and PPR > 1 is considered as PPF. PPF is a dynamic enhancement process of neurotransmitter release, which is considered to be the key to the processing of visual and auditory information at biological synapses [1, 63]. It reflects the ability of biological synapses to receive information during information processing. Therefore, simulating the PPF function of biological synapses in neuromorphic devices is a crucial step in the development of artificial neural networks.

In view of the above understanding of the STP of biological synapses, we studied the EPSP behavior of the paper-based artificial synaptic device under paired-pulse stimulation, as shown in Figs. 2(d) and 2(e). It can be observed that under paired-pulse displacement stimulation intensity (d = 1 mm) with a very short interval time (Δt = 0.91 s), the device exhibits a typical PPF phenomenon, that is, the amplitude of the peak voltage for the second EPSP (A_2 = 12.573 V) is greater than that of the first EPSP (A_1 = 1.445 V) (Fig. 2(e)). In paper-based artificial synaptic devices, the observed enhancement of EPSP under successive mechanical stimulation originates from interfacial residual charge

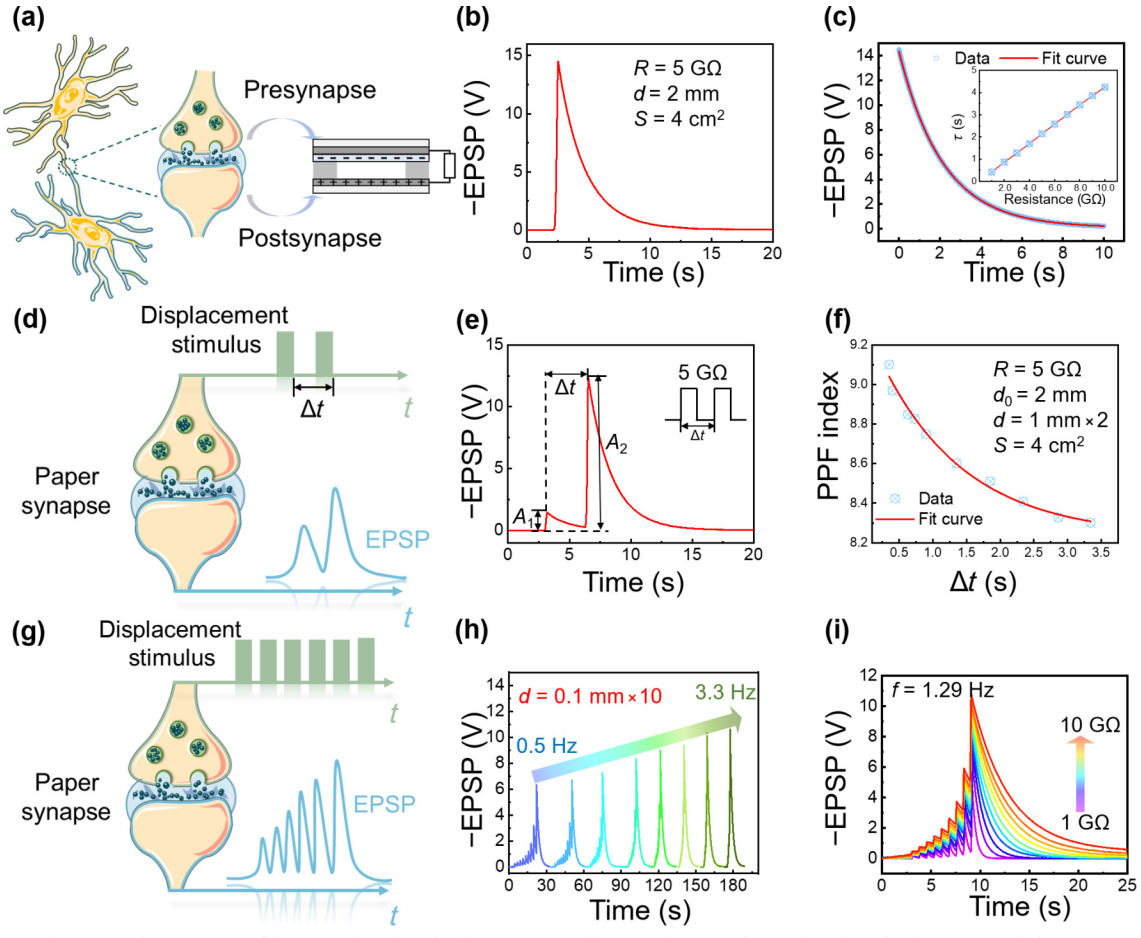

Figure 2 Typical synaptic characteristics of the paper-based artificial synapse. (a) Schematic diagram of paper-based artificial synapse, and the corresponding signal transmission from pre-synapse to post-synapse in biosomes. (b) The EPSP responses under a displacement stimulus. (c) The decay phenomenon fitting of the EPSP with the exponential decay model. The inset is the value of resistance relation to the value of τ. (d) Schematic illustration of EPSPs activated by paired-pulse displacement stimulus. (e) The typical EPSP responses under d = 1 mm and Δt = 0.91 s. (f) The PPF index (defined as the ratio of A_2/A_1) versus interval time between successive pulses. (g) Schematic illustration of EPSPs activated by multiple displacement stimulation. (h) EPSPs recorded in response to the different frequencies of displacement stimuli, from 0.5 to 3.3 Hz. Each frequency consisted of 10 displacement stimuli of 0.1 mm with a series resistance value of 5 GΩ. (i) EPSP of the paper-based artificial synapse versus different values of resistance, from 1 to 10 GΩ. The displacement stimulation intensity was 0.2 mm and the number of movements was 10.

accumulation. Initially, the electrode potential difference maintains equilibrium. Upon initial mechanical displacement, the interelectrode distance modulation establishes a potential gradient that drives charge redistribution, creating localized negative and positive charge accumulation at respective electrodes. Subsequent rapid mechanical stimuli prevent complete charge recombination through the load resistance, leaving residual interfacial charges. This charge accumulation mechanism enables progressive polarization enhancement during consecutive stimuli—the second displacement further increases charge separation magnitude, thereby amplifying EPSP amplitude. Such cumulative polarization effects fundamentally underlie PPF and short-term memory behaviors in these synaptic devices.

The PPF index, defined as $A_2/A_1 \times 100\%$, quantifies synaptic facilitation strength. When the Δt is varied under identical conditions, the PPF index increases as Δt shortens. To analyze this behavior, the experimental data were fitted with a double-exponential decay function, as its dynamics closely resemble the response patterns of biological neural synapses. The fitting results demonstrate excellent agreement between the fitted curve and experimental data (denoted by the red curve) [62–64]. The double-exponential function used to fit the PPF index (y) is expressed as follows

$$y = C + A_1 \times \exp\left(-\frac{\Delta t}{t_1}\right) + A_2 \times \exp\left(-\frac{\Delta t}{t_2}\right) \quad (4)$$

where t_1 and t_2 are the relaxation times. According to the fitting results, the t_1 and t_2 values are 0.51 and 1.84 s, respectively, which are compatible with biological synapses.

As shown in Fig. 2(f), when the interval time is 0.35 s, the PPF index is 9.1, which is much higher than that of other synaptic devices. When the interval is increased to 3.4 s, the second peak voltage is still much higher than the first peak voltage (A_2/A_1 = 8.3). In this regard, the effects of different d and different original separation positions (d_0) on PPF were further studied, as shown in Fig. S6 in the ESM. It was found that at the same d (d = 1 mm), with the increase of d_0, both A_1 and A_2 decreased, but A_2 decreased much more than A_1 (Fig. S6(a) in the ESM). Accordingly, corresponding PPF index also showed a decreasing trend (Fig. S6(b) in the ESM). It indicates that the electrostatic charges driven by applying the same displacement stimulus in the relatively large separation distance are smaller than those in the relatively small separation distance. Therefore, decreasing the original separation position can obtain a larger PPF index. Under the condition of the same original separation position (d_0 = 2 mm), when d increased, both A_1 and A_2 increased, but A_2 increased more than A_1 (Fig.

S6(c) in the ESM). In this case, the PPF index showed an increasing trend (Fig. S6(d) in the ESM). This indicates that the larger the applied displacement stimulus, the larger the EPSP obtained under the same original separation position. It was learned that even though the same displacement stimulus was applied, if the second displacement stimulus was applied closer than the first relative position, the increment of A_2 was greater. Accordingly, increasing the intensity of the displacement stimulus and decreasing the original separation distance within a controlled operating range can result in a larger paired-pulse gain effect.

Through systematic experimental validation, the unique advantages of paper-based artificial synaptic devices in the field of neuromorphic computing have been further elucidated. These results reconfirm the robust PPF effect exhibited by the proposed device. Additionally, the PPF values under varying resistance conditions were investigated (Fig. S7 in the ESM). It was observed that the PPF curve shifts upward with increasing resistance. This phenomenon indicates that higher resistance not only reduces leakage current and prolongs the relaxation time of charge migration but also enhances charge trapping capability, thereby establishing a sustained localized electric field. Such a field amplifies the synergistic interaction between preceding and subsequent pulses. These findings provide critical guidance for developing environmentally adaptive neuromorphic devices with enhanced performance.

In the nervous system, synaptic efficacy can be enhanced within milliseconds after a specific brief stimulus (i.e., synaptic plasticity). As a result of enhanced STP, synapses can be used to dynamically filter the transmitted information depending on signal frequency. STP results in high-pass filtering, where high-frequency signals pass normally during signal transmission, while low-frequency signals below a set threshold are attenuated or even blocked. Figures 2(g) and 2(h) show the responses of paper-based artificial synapses to different frequencies of displacement stimuli, each consisting of 10 displacement stimuli of 0.1 mm with a series resistance value of 5 GΩ. The results show that the peak of EPSP increases significantly with increasing frequency. When the frequency is 0.5 Hz, the peak of EPSP is 6.322 V; when the frequency increases to 3.3 Hz, the peak of EPSP grows to 10.708 V. This indicates that the device can be used as a dynamic high-pass filter, which is the key to artificial neural networks.

In addition to this, we also explored the effect of varying series-resistances on the EPSP peaks under multiple displacement pulse stimuli. As shown in Fig. 2(i), we kept a frequency of 1.29 Hz and each motion consisted of 10 displacement stimuli of 0.2 mm. As the resistance value increases (from 1 to 10 GΩ), the peak EPSP increases from 5.376 to 10.826 V. This indicates that changing the resistance value can well increase the peak EPSP of multiple pulses. Given the contact–separation mode of the device, we investigated the stability of the device under multiple contact–separation conditions (multi-pulse displacement stimulation), as shown in Fig. S8 in the ESM. A paper-based artificial synaptic device with a size of 20 mm × 20 mm, a series resistance value of 5 GΩ, a displacement stimulus intensity of 0.2 mm, 10 movements, and a movement frequency of 1.29 Hz was applied to the experiment. Corresponding EPSPs have been monitored in real time for 50 cycles and largely overlapped during the cyclic displacement stimulation, indicating that the paper-based artificial synaptic device has good mechanical reliability.

2.3 Characterization of spatiotemporal synaptic properties of paper-based artificial synapses

A single excitatory synaptic device has a paired-pulse susceptibility phenomenon and high-pass filtering effect. Multiple excitatory synaptic devices can receive temporally and spatially correlated stimuli from different neurons, which in turn induce postsynaptic neurons to establish dynamic logic. The EPSP difference between synapses 2 and 1 ($\Delta EPSP_{pre2-pre1}$) between two distinguishable displacement stimuli is considered to be the key spatiotemporal trigger source. We used two paper-based artificial synaptic devices to simulate spatiotemporal dynamic logic, as shown in Fig. 3(a). All tests were performed with a series resistance value of 5 GΩ and the size of the device of 20 mm × 20 mm. When a displacement stimulus (d = 2 mm) is applied to the presynaptic membrane of the device, the electrostatic charges will be driven to the contact interface and trigger the EPSP.

As shown in Fig. 3(b), one displacement stimulus applied to synapse 1 (d_x = 2 mm) will trigger $EPSP_1$ with an amplitude of 14.5 V. The other displacement stimulus applied to synapse 2 (d_y = 2 mm) will trigger $EPSP_2$ with an amplitude of 14.5 V. When $\Delta t_{pre2-pre1} = -1$ s, the $EPSP_2$ will superimpose with $EPSP_1$ and contribute to $EPSP_1$, leading to an enhanced $EPSP_1$ > 14.5 V. $EPSP_1$ increases as the $\Delta t_{pre2-pre1}$ decreases. When two displacement stimuli are applied simultaneously to synapses 1 and 2 ($\Delta t_{pre2-pre1} = 0$), the charge migrating to the interface region will be accumulated, and therefore the two EPSPs will be superimposed (EPSPs = 29.0 V). When the displacement stimulus was applied to synapse 2 later than synapse 1 (i.e., $\Delta t_{pre2-pre1}$ = +1 s), the later stimulus had no contribution to $EPSP_1$, resulting in unchanged $EPSP_1$ = ~ 14.5 V. The temporal modulation of EPSP amplitude in subsequent synaptic events arises from interfacial charge accumulation dynamics. Upon mechanical stimulation of synapse 1, the induced potential gradient facilitates charge transfer across the electrode interface, resulting in postsynaptic membrane depolarization through positive charge accumulation. When the interstimulus interval falls below the characteristic charge recombination time, the secondary stimulation on synapse 2 interacts synergistically with residual charges from the initial event. This spatiotemporal overlap of charge distributions produces constructive interference, leading to EPSP amplitude potentiation.

Such summation is a dynamic analogue function of time and $\Delta t_{pre2-pre1}$. The effect of the second presynaptic pulse displacement stimulus becomes greater when the $\Delta t_{pre2-pre1}$ between the displacement stimuli applied to the two synapses is changed. The effect of the second presynaptic pulse displacement stimulus on the first pulse displacement stimulus is assessed using the first recorded EPSP, as shown in Fig. 3(c). If synapse 2 is triggered after synapse 1 ($\Delta t_{pre2-pre1} > 0$), the amplitude of $EPSP_1$ is the same as the amplitude of synapse 1 alone. In contrast, when synapse 2 is triggered before synapse 1 ($\Delta t_{pre2-pre1} < 0$), $EPSP_1$ is influenced by synapse 2 and the amplitude of $EPSP_1$ increases.

We also investigated the relationship between $\Delta EPSP_{pre2-pre1}$ and $\Delta t_{pre2-pre1}$, as shown in Fig. 3(d). When $\Delta t_{pre2-pre1} < 0$, $EPSP_1$ triggers after $EPSP_2$, and $EPSP_2$ basically maintains at 14.5 V. $EPSP_1$ is influenced by $EPSP_2$ and gradually increases as the time interval decreases, so $\Delta EPSP_{pre2-pre1}$ negatively increases. When $\Delta t_{pre2-pre1} > 0$, $EPSP_1$ triggers before $EPSP_2$ and $EPSP_1$ basically maintains at 14.5 V. Although $EPSP_2$ is more than 14.5 V, which is influenced by $EPSP_1$, the superposition effect of $EPSP_2$ decreases as the time interval grows, so $\Delta EPSP_{pre2-pre1}$ positively decreases.

In addition, we also investigated the behavior of paper-based artificial synaptic devices in other conditions. We applied different d (d_x = 1 mm and d_y = 5 mm) to two devices and investigated their associated spatiotemporal dynamic logic, as shown in Figs.

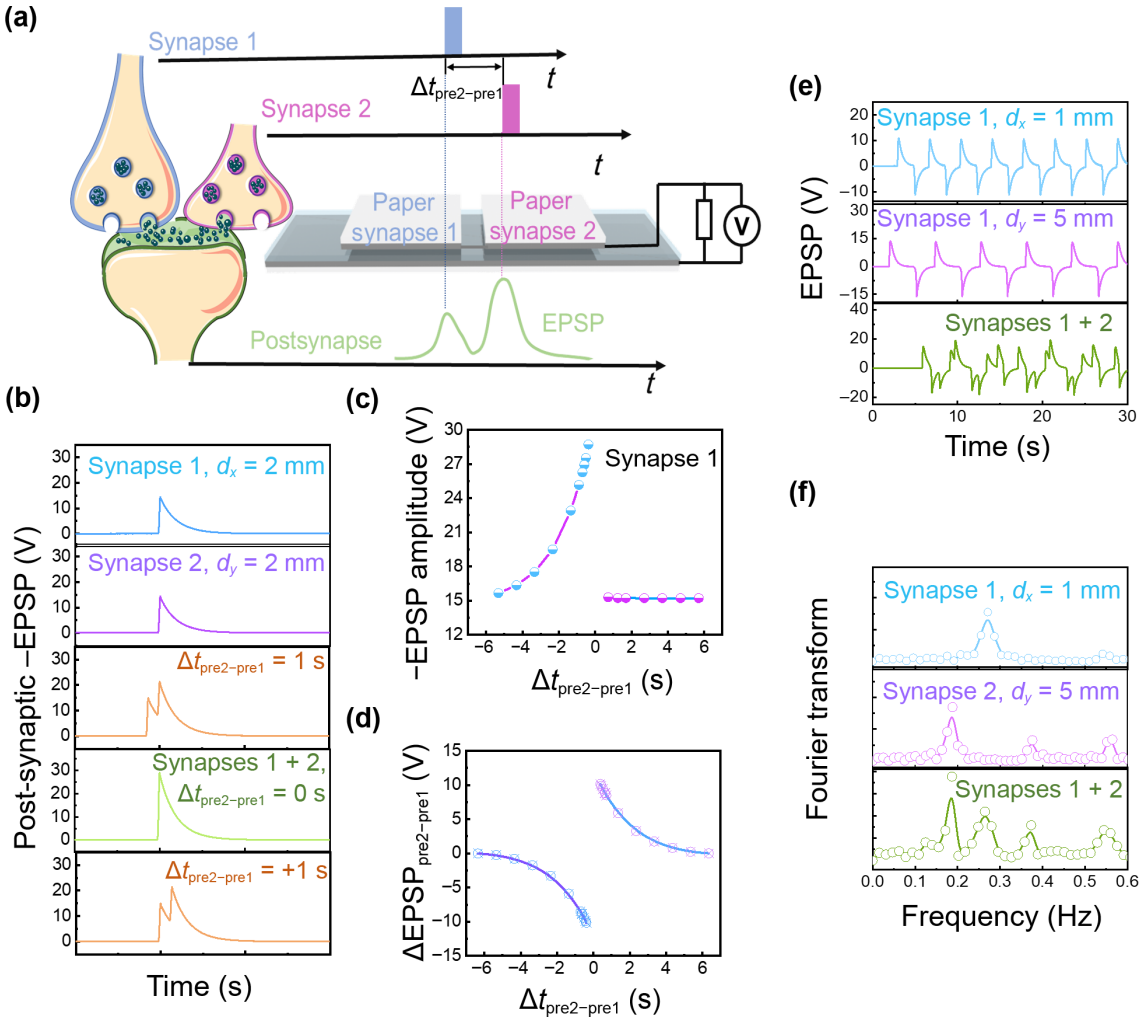

Figure 3 The advanced spatiotemporal synaptic characteristics of the paper-based artificial synapse. (a) Schematic illustration of EPSPs activated by dual paper-based artificial synapses. (b) EPSPs activated by single and paired displacement stimulation with spatiotemporal information. (c) Amplitude of the EPSPs of paper synapse 1 versus $\Delta t_{pre2-pre1}$ between the first and second displacement stimulation. (d) $\Delta EPSP_{pre2-pre1}$ versus $\Delta t_{pre2-pre1}$. (e) Original data of Fourier transform of paper-based artificial synaptic devices. EPSP with a 1 mm displacement stimulus applied to paper-based artificial synaptic device 1. EPSP with a 5 mm displacement stimulus applied to paper-based artificial synaptic device 2. (f) The extracted frequencies paper-based artificial synaptic device 1 and activations after Fourier transform.

S9(a)–S9(d) in the ESM. We designed two devices with different area sizes (S_x = 5 mm × 5 mm and S_y = 30 mm × 30 mm) to investigate their time-related behaviors, as shown in Figs. S9(e)–S9(i) in the ESM. When the device size is different or the intensity of displacement stimuli is different, it can still recognize the temporal–spatial order, which is similar to the transmission of signals at different biological synapses. It shows that our paper-based artificial synaptic devices can well simulate the spatiotemporal dynamic logic, which lays a solid foundation for the subsequent establishment of artificial neural networks.

Beyond dynamic logic associated with temporal intervals, the identification of external stimulus frequency and magnitude holds significant importance. As shown in Figs. 3(e) and 3(f), real-time EPSPs were monitored for two paper-based artificial synaptic devices under displacement stimuli of varying intensities (d_x = 1 mm and d_y = 5 mm) and frequencies. Paper-based artificial synaptic device 1 exhibited EPSPs under a 1 mm displacement stimulus, and paper-based artificial synaptic device 2 exhibited EPSPs under a 5 mm displacement stimulus (both devices under simultaneous displacement stimuli, Fig. 3(e)). By analyzing the spatiotemporal patterns of postsynaptic voltage through Fourier transformation, both the frequency and amplitude of the displacement stimuli applied to the devices were successfully identified (Fig. 3(f)). The Fourier transformed results aligned with the original and combined datasets. Paper-based artificial synaptic device 1 displayed a stimulus frequency of 0.271 Hz, and paper-based artificial synaptic device 2 displayed a stimulus frequency of 0.187 Hz, both of which were consistent with the actual testing parameters. This confirms the method's capability to resolve frequency-dependent amplitude variations, highlighting the devices' exceptional temporal discrimination capability. This experiment simulated the dendritic integration of action potentials from multiple presynaptic neurons to a postsynaptic neuron—a mechanism critical for the tactile acuity of slowly adapting type I (SA-I) afferent nerves in advanced biological systems. Such functionality is pivotal for mimicking biomimetic sensory processing in neuromorphic engineering.

2.4 Neuromorphic computation based on paper-based artificial synaptic devices

The von Neumann architecture suffers from a memory bottleneck in hardware platforms, leading to high energy consumption and slow processing speeds when handling data-intensive computational tasks. Current solutions employ graphics

processing units for parallel data processing or application-specific integrated circuits optimized for dataflow, yet these accelerators still maintain spatial separation between memory and computing units [7, 53, 62, 64]. In contrast, the human brain—with its massive parallelism, adaptability, and self-learning capabilities—eliminates this distinction: Information storage occurs via neurons and synapses, enabling in-memory computing where data storage and logic operations coexist spatially. This inherent advantage positions neuromorphic devices as a transformative solution for in-memory computing architectures [65–67]. TENGs can directly convert external dynamic mechanical stimuli into electrical signals. Crucially, under no-load conditions, the potential distribution generated by mechanical displacement stimuli remains confined within the material's internal structure, endowing TENGs with mechanical in-memory computing capabilities. Building on this principle, the paper-based artificial synaptic device demonstrates synaptic nonvolatility and the potential to execute Boolean logic operations. By modulating the direction of displacement stimuli to alter output voltages, this device achieves integrated data storage and computational functionality. These findings validate its capability to unify memory and computation—a critical advancement for next-generation neuromorphic systems.

Figure 4(a) presents the circuit schematic of a paper-based artificial synaptic device, where the logic state is determined by the output potential difference (V_{out}) between its electrodes. The coupled triboelectric–electrostatic effects generate V_{out} upon mechanical displacement. Following binary computation conventions, we defined V_{out} < 0 V as logic "1". Circuit reconfiguration via a single-pole double-throw (SPDT) switch (Terminal 1–2 ↔ 1'–2') inverts the potential difference, enabling logic state switching. This mechanism enables successful implementation of an "NOT" logic gate based on the paper-based artificial synaptic device, demonstrating the capability of Boolean logic operations (truth table of the NOT logic gate in Fig. 4(b)). When connected to Terminal 1–2, a –0.5 mm displacement (from the preset separation distance d_0 = 1 mm) yields V_{out} < 0 V (logic "0"). Open-circuit conditions maintain this state (Fig. 4(c)(1), blue region), while a 5 GΩ series resistor causes voltage to gradually decay to baseline in 8 s (Fig. 4(c)(2), blue region). Conversely, +0.5 mm displacement produces V_{out} ≥ 0 V (logic "1"), maintained temporarily in open-circuit (Fig. 4(c)(1), white region) or decaying with series-resistor situation (Fig. 4(c)(2), white region). Terminal 1'–2' connection under the same condition (d_0 = 1 mm and d = –0.5 mm) inverts these responses (Fig. 4(c)(1)), consistent with the signal mechanism of paper-based TENG devices and paper-based artificial synaptic devices (Fig. S1 in the ESM). Reconfiguring the connection polarity of a single paper-based artificial synapse enables a NOT gate operation and validates its memory-computation capabilities.

The integration of two paper-based artificial synaptic devices can further help to implement "AND" logic gate and "NAND" logic gate through forward and reverse circuit configurations (schematic diagram in Fig. 4(d)). We configured two devices with different initial separations (d_{x0} = 0.5 mm and d_{y0} = 1 mm) and applied four displacement stimulus combinations: (0, 0) yielding

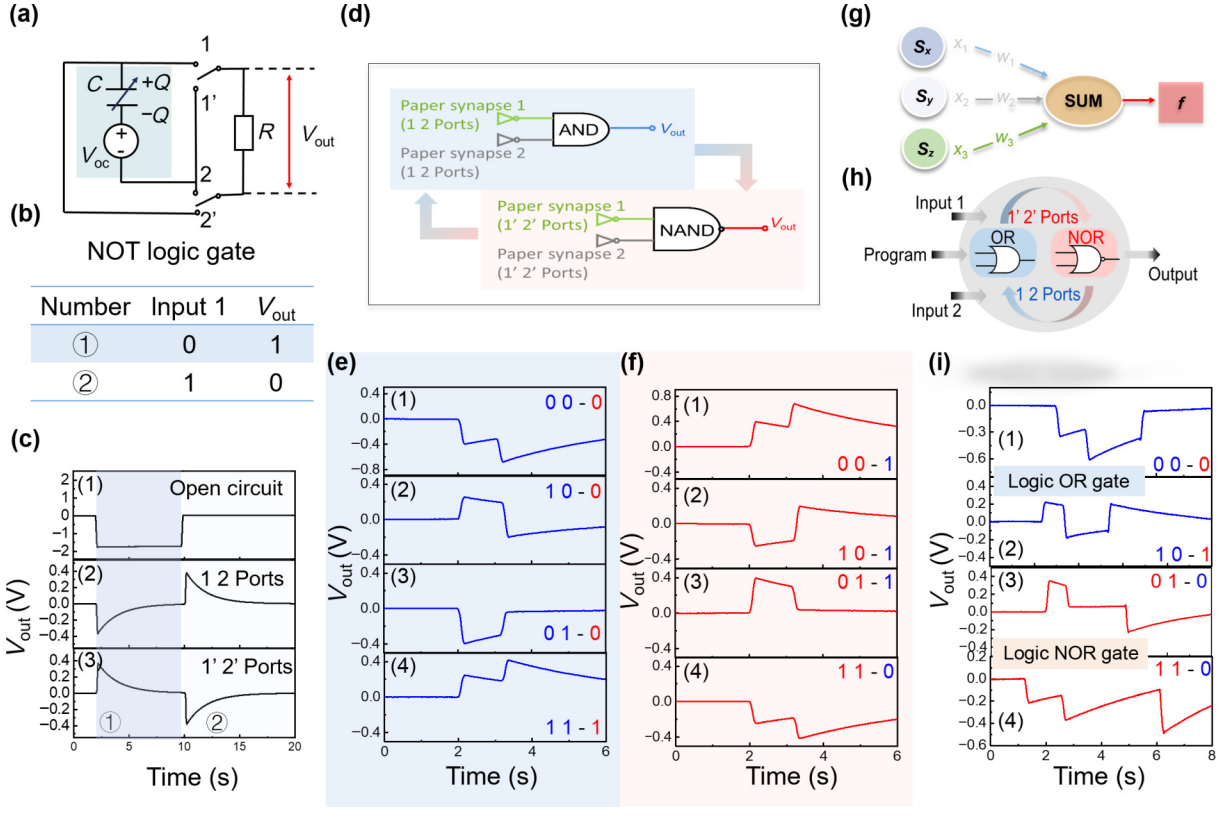

Figure 4 The simple logic gate system based on paper-based artificial synapses. (a) Basic circuit diagram of the logic NOT gate (when the circuit is connected to 1 Port and 2 Port is positive connection, when the circuit is connected to 1' Port and 2' Port is reverse connection). (b) The truth tables of logic NOT gate upon single paper-based artificial synaptic input voltages. (c) The output voltage of the logic NOT gate measured at different input states. Output voltage less than 0 V is logic "0", output voltage greater than or equal to 0 V is logic "1". (d) Schematic diagram of the logic AND gate and logic NAND gate operation switching. (e) The output voltage of the logic AND gate based on double paper-based artificial synaptic devices. (f) Logic NAND gate signal based on double paper-based artificial synaptic devices. (g) The flowsheet of computing logic OR gate. (h) Schematic diagram of the logic OR and NOR gate operation switching. (i) The output voltage of the logic OR gate and logic NOR gate based on triple paper-based artificial synaptic devices.

V_{out} = −0.668 V (logic "0", Fig. 4(e)(1)); (1, 0) producing −0.199 V (logic "0", Fig. 4(e)(2)); (0, 1) generating −0.301 V (logic "0", Fig. 4(e)(3)); and (1, 1) resulting in logic "1" (Fig. 4(e)(4)). This behavior precisely matches AND gate characteristics (truth table in Fig. S10(a) in the ESM), with comparative state analyses shown in Figs. S10(b)–S10(i) in the ESM. All measurements employed a 5 GΩ series resistor, though open-circuit configurations may offer superior information storage potential.

Building upon our implementations of NOT, AND, and NAND gates, we extended the system to realize more complex "OR" and "NOR" logic gates through the incorporation of a programmable unit (Fig. 4(g)). The circuit architecture comprises two operational units (S_x, S_y) activated by displacement stimuli (d_x, d_y), and a programming unit (S_z) with fixed displacement (d_z = +0.5 mm). Thus, the logical OR gate and logical NOR gate can be implemented by forward and reverse connections as shown in Fig. 4(h). We prepared three paper-based artificial synaptic devices; all these devices are set at the same original separation position (d_{x0} = d_{y0} = d_{z0} = 1 mm), and the program unit applies a displacement stimulus d_z = +0.5 mm at constant speed. When a displacement stimulus of (0, 0), i.e., d_x = −0.5 mm and d_y = −0.5 mm is applied to the device, V_{out} is −0.389 V (logical "0"), as shown in Fig. 4(i)(1). When a displacement stimulus of (0, 1), namely, d_x = −0.5 mm and d_y = +0.5 mm, is applied to the device, V_{out} = 0.236 V (logic "1"), as shown in Fig. 4(i)(2). If the device is stimulated with (1, 0), that is, d_x = +0.5 mm and d_y = −0.5 mm, V_{out} is 0.207 V (logic "1"). When the displacement stimulus of (1, 1) is applied to the device (i.e., d_x = +0.5 mm and d_y = +0.5 mm), logic "1" is achieved with V_{out} = 0.491 V. The truth table of the logical OR gate and the signal in the open-circuit state are shown in Fig. S11 in the ESM. By reversing the circuit, we successfully implemented the logical "NOR" gate, as shown in Figs. 4(i)(3) and 4(i)(4).

The paper-based artificial synaptic logic gates demonstrate a viable in-memory computing framework for implementing Boolean logic operations in flexible electronics. This achievement is enabled through innovative circuit architecture design and dynamic parameter modulation strategies. Notably, logical conversion—such as OR-to-NOR gate conversion—is accomplished via circuit reconfiguration, with output responses (0 ↔ 1) exhibiting perfect truth table correspondence, thereby confirming the system's programmable multifunctionality. Four key parameters govern the logic operations: initial electrode separation distance, applied mechanical displacement, load resistance, and device configuration. Importantly, the paper substrate's inherent biodegradability and low-cost fabrication, combined with the synaptic devices' neuromorphic response characteristics, present unique opportunities for developing sustainable implantable bioelectronics and environmentally-conscious intelligent hardware systems that merge ecological considerations with neuromorphic computing capabilities.

2.5 Three-dimensional information transfer based on paper-based artificial synaptic devices

Synapses serve as fundamental biological units that mediate information transfer and modulate connection strength between pre- and post-synaptic neurons. These processes underlie critical neural functions, including environmental perception, associative learning, parallel computation, and motor command execution [68–70]. To overcome the limitations of single synaptic units in complex information processing, we developed a three-layer paper-based artificial synaptic device capable of multi-level signal transmission [71–75]. The artificial neural network architecture, illustrated in Fig. 5(a), mimics the three-neuron biological circuit. In native systems, suprathreshold stimuli trigger neurotransmitter release from the presynaptic membrane, inducing EPSPs through plasticity-related protein diffusion and ion channel activation (Fig. 5(a)(1)). These EPSPs propagate information to downstream synapses when exceeding the action potential threshold (Fig. 5(a)(2)), while subthreshold responses result in signal termination (Fig. 5(a)(3)).

We developed a vertically-stacked three-layer paper-based artificial synaptic device to emulate biological synaptic information transfer. The device architecture (Fig. S12 in the ESM) enables mechanical coupling between layers. Displacement stimuli applied to the first synaptic layer (Syn1) propagate partially to subsequent layers (Syn2 and Syn3), effectively mimicking stimulus dependent neural signal transmission. By applying varying displacement stimuli (0.1–1.0 mm) to the three-layer paper-based artificial synaptic device, we validated interlayer signal transmission efficacy through EPSP measurements. Syn1 exhibited EPSP modulation from −0.166 to −15.226 V (Fig. S13 in the ESM), with sensitivity coefficients (K) exhibiting nonlinear decay across three displacement stages (Fig. 5(b)). In the 0.1–0.4 mm range (Stage 1), the system demonstrated high sensitivity (K_{1-1} = 23.023), followed by reduced sensitivity (K_{1-2} = 16.099 in the 0.4–0.7 mm range (Stage 2), and further attenuation (K_{1-3} = 10.38) at 0.7–1.0 mm (Stage 3). Syn2 demonstrated similar displacement-stage correspondence (Fig. 5(c)), with EPSP ranging from −0.015 to −14.258 V (Fig. S14 in the ESM), with sensitivity coefficients K_{2-1} = 15.717, K_{2-2} = 23.601, and K_{2-3} = 9.276. Notably, Syn3 showed enhanced late-stage sensitivity (K_{3-3} = 27.261) during 0.7–1.0 mm displacements (Fig. 5(d)), with EPSP progression from 0 to −13.712 V (Fig. S15 in the ESM).

The experimental results demonstrate threshold-dependent signal propagation characteristics in the trilayered synaptic architecture. At stage 1 (0.3 mm displacement), Syn1 achieved maximum sensitivity (K_{1-1} = 23.023) with $EPSP_1$ = −9.688 V, while Syn2 and Syn3 remained unresponsive ($EPSP_2$ ~ 1 V and $EPSP_3$ <1 V), indicating incomplete signal transmission (Fig. S16(a) in the ESM). Progressing to stage 2 (0.5 mm), Syn2 displayed peak sensitivity (K_{2-2} = 23.601) with $EPSP_2$ = −6.367 V, confirming successful Syn1 → Syn2 transmission while Syn3 maintained inactivity (Fig. S16(b) in the ESM). At stage 3 (0.8 mm), complete synaptic connectivity was established, with Syn3 exhibiting optimal sensitivity (K_{3-3} = 27.261) and measurable $EPSP_3$ = −9.468 V, alongside enhanced responses from upstream synapses ($EPSP_1$ = −13.238 V and $EPSP_2$ = −12.495 V) (Fig. S16(c) in the ESM). This displacement-gated transmission mechanism enables programmable information routing: Syn1 activation requires ≥ 0.3 mm stimuli, Syn1 → Syn2 transmission necessitates ≥ 0.5 mm displacements, and full Syn1 → Syn2 → Syn3 connectivity is achieved at ≥ 0.7 mm. The graded response profiles confirm the device's capability for stimulus-intensity-modulated signal processing. These results highlight displacement-tunable hierarchical information routing in the trilayered synaptic device.

As a proof-of-concept demonstration, we fabricated a three-layer paper-based artificial synaptic array capable of programmable information processing through spatially-controlled mechanical stimuli. When uniformly activated by 1 mm displacements across all loci (Fig. 5(e)), the device exhibits complete synaptic connectivity and efficient signal transmission. Differential stimulation enables selective layer-to-layer

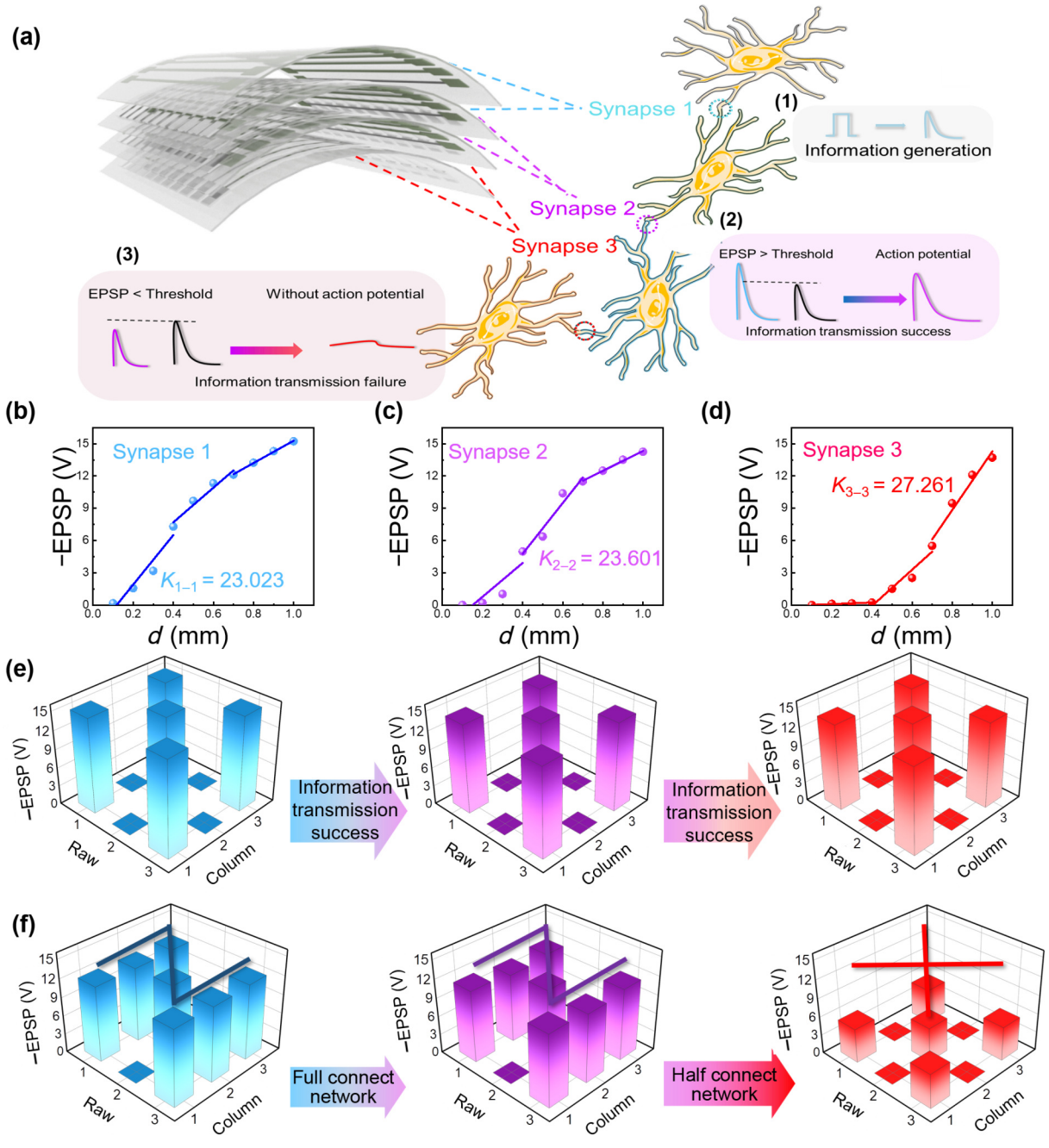

Figure 5 Information transmission emulated by the three-layer paper-based artificial synaptic array devices. (a) Structure diagram of an artificial neural network consisting of three-layer paper-based artificial synaptic arrays that correspond to three-level neurons. (1) Information generation. (2) Information transmission success. (3) Information transmission failure. (b)–(d) The relationship between EPSP and displacement stimulation for Syn1, Syn2, and Syn3 in the signal three-layer paper-based artificial synaptic device. (e) For the three-layer paper-based artificial synaptic arrays devices and information transmission success. (f) For the three-layer paper-based artificial synaptic arrays devices, full connect network, and half connect network.

connectivity, as demonstrated by applying 0.7 and 0.5 mm displacement stimuli (Fig. 5(f)). This configuration establishes full Syn1 → Syn2 connectivity, enabling accurate recognition and transmission of the "N" pattern, while maintaining partial Syn2 → Syn3 connectivity due to threshold effects. Consequently, Syn3 only processes signals from 0.7 mm-stimulated regions, yielding an "X" output pattern. The observed 3D synaptic transmission mechanism enables direct modulation of connectivity states through quantifiable physical parameters (displacement intensity/spatial distribution). This bioinspired design overcomes limitations of conventional electrically-modulated neuromorphic devices, establishing a novel platform for developing environment-adaptive intelligent systems. The graded activation thresholds (Syn1: 0.3 mm and K_{1-1} = 23.023; Syn2: 0.5 mm and K_{2-2} = 23.601; and Syn3: 0.7 mm and K_{3-3} = 27.261) mimic biological temporal summation effects, enabling cumulative signal amplification through sequential subthreshold stimuli. This physics-driven paradigm allows dynamic adjustment of feature weights and functional mappings, as evidenced by the coexistence of full Syn1 → Syn2 connectivity with partial Syn2 → Syn3 transmission.

Comparative analysis with state-of-the-art triboelectric artificial synaptic devices (Table S1 in the ESM [5, 7, 62, 76–81]) reveals several distinctive advantages of our approach. Material-wise, our device achieves synaptic functionality using significantly simplified

material composition. In terms of mechanism, whereas conventional triboelectric transistors require TENG-mediated transistor modulation, our design enables direct resistive regulation of non-volatile triboelectric charges. The device exhibits exceptional retention characteristics spanning milliseconds to hours, addressing diverse application requirements, including long-term information storage. Functionally, it demonstrates comprehensive logic gate implementation (AND, OR, NAND, NOR), showcasing superior compatibility with advanced computing architectures. These collective advantages in material simplicity, operational mechanism, synaptic plasticity, retention performance, and functional versatility position our technology as a promising candidate for next-generation triboelectric neuromorphic systems.

3 Conclusions

In summary, we developed a vertically integrated paper-based artificial synaptic device that utilizes TENG principles of contact electrification and electrostatic induction mechanisms. The device accurately reproduces essential biological synaptic functions through controlled mechanical displacement stimuli, demonstrating key neuro-mimetic behaviors, including EPSP and PPF, while exhibiting spatiotemporally modulated high-pass filtering characteristics. The vertical contact architecture yields enhanced PPF indices, surpassing conventional planar configurations. Through strategic circuit reconfiguration, we achieved fundamental logic operations (NOT gates) and their lateral combinations (AND, NAND, OR, NOR gates), demonstrating exceptional functional programmability within a mechanically simple framework suitable for flexible in-sensor computing applications. Our 3D-stacked trilayer architecture represents a significant advancement, enabling biomimetic multilevel signal transmission with biological fidelity. The device exhibits stimulus-intensity-dependent graded responses and unique spatial programmability, selectively establishing full (≥ 0.7 mm) or partial (0.3–0.7 mm) synaptic connectivity through localized displacement modulation. This mechanoelectrical coupling paradigm pioneers an eco-friendly platform for biodegradable neuromorphic systems, with promising applications in adaptive robotics and intelligent wearables.

The self-powered artificial synapses are transforming tactile perception paradigms through synergistic integration of biological neural processing mechanisms with advanced high-entropy energy-harvesting technologies. Three key advancements demonstrate their transformative potential: (1) Enhanced biomimetic tactile sensors that replicate skin mechanoreceptor dynamics while preserving spatiotemporal stimulus information [73]. (2) Multimodal neuromorphic perception systems combining mechanical and photonic plasticity through phototransistor integration [57]. (3) Energy-efficient neuromorphic architectures utilizing TENGs for direct mechanoelectrical conversion, significantly reducing synaptic power consumption [62]. These innovations collectively enable the transition from passive tactile data acquisition to intelligent responsive systems through their unique combination of energy autonomy and neural-inspired information processing.

Future research directions for the paper-based neuromorphic systems may focus on three transformative approaches: (1) Development of distributed neuromorphic networks utilizing flexible synaptic arrays to emulate skin-like perceptual decision-making processes. (2) Implementation of biologically inspired multisensory integration combining tactile, visual, auditory, gustatory, and olfactory modalities for interactive perception. (3) Advancement of self-sustaining neuromorphic architectures, including implantable devices powered by biological energy sources (e.g., vascular pulsations) and environmentally powered systems harnessing mechanical vibrations for autonomous online learning.

4 Experiments

4.1 Fabrication of the single paper-based artificial synapse device

First, CNT ink was deposited onto A4-sized Teslin paper via rod coating method. The CNT-coated substrate was then oven-dried at 130 °C for 15 min to establish a uniform conductive layer. Then, laser cutting was employed to section the cured CNT paper into 20 mm × 20 mm squares. An FEP film was laminated onto one CNT sheet as the postsynaptic membrane, while a bare CNT sheet served as the presynaptic membrane. Finally, a programmable weight adjustment mechanism was implemented by connecting a tunable resistor between the CNT and FEP–CNT sheets. Structural integrity was ensured using 3M tape as a spacer layer, enabling precise alignment of the presynaptic and postsynaptic components.

4.2 Fabrication of the single multilayer paper-based artificial synapse device

First, following the aforementioned procedure, single-sided CNT paper and double-sided CNT paper were prepared. The prepared CNT paper was then laser-cut into approximately 15 mm × 15 mm squares. FEP films were laminated onto the single-sided CNT paper and one side of the double-sided CNT paper. Next, the CNT paper, FEP-laminated single-sided CNT paper, and FEP-laminated double-sided CNT paper were alternately stacked. Interlayer adhesion was achieved using 3M tape with a thickness of 0.1 mm, ensuring stable interlayer spacing while maintaining the device's flexibility. Finally, resistors were connected between the presynaptic and postsynaptic layers in each stratum to enable spatially programmable synaptic weights.

4.3 Device characterizations

Material morphology and structure were characterized using a Nova field emission scanning electron microscope. All electrical characteristics of the paper-based artificial synaptic devices were measured by a Keithley 6514 electrometer at room temperature in air. The motion of the paper-based artificial synaptic devices was controlled by a displacement table. All displacement table motion conditions were acceleration of 50 mm/s^2 and velocity of 20 mm/s.

Acknowledgements

This work is financially supported by the National Key Research and Development Program from Ministry of Science and Technology (No. 2023YFB3208102), the National Natural Science Foundation of China (No. 52073031), and the "Hundred Talents Program" of the Chinese Academy of Sciences.

Electronic Supplementary Material: Supplementary material (working mechanism, SEM characterization, material thickness testing, reliability tests, and logic gate and the three-layer paper-

based artificial synaptic device) is available in the online version of this article at https://doi.org/10.26599/NRE.2025.9120187.

Declaration of conflicting interests

The authors declare no conflicting interests regarding the content of this article.

Data availability

All data needed to support the conclusions in the paper are presented in the manuscript and/or the Supplementary Materials. Additional data related to this paper may be requested from the corresponding author upon request.

References

[1] Yu, J. R.; Wang, Y. F.; Qin, S. S.; Gao, G. Y.; Xu, C.; Lin Wang, Z.; Sun, Q. J. Bioinspired interactive neuromorphic devices. *Mater. Today* **2022**, *60*, 158–182.

[2] Chouhdry, H. H.; Lee, D. H.; Bag, A.; Lee, N. E. A flexible artificial chemosensory neuronal synapse based on chemoreceptive ionogel-gated electrochemical transistor. *Nat. Commun.* **2023**, *14*, 821.

[3] Matrone, G. M.; Bruno, U.; Forró, C.; Lubrano, C.; Cinti, S. ; van de Burgt, Y.; Santoro, F. Electrical and optical modulation of a PEDOT:PSS-based electrochemical transistor for multiple neurotransmitter-mediated artificial synapses. *Adv. Mater. Technol.* **2023**, *8*, 2201911.

[4] Lin, X. D.; Feng, Z. Y.; Xiong, Y.; Sun, W. W.; Yao, W. C.; Wei, Y. C.; Wang, Z. L.; Sun, Q. J. Piezotronic neuromorphic devices: Principle, manufacture, and applications. *Int. J. Extrem. Manuf.* **2024**, *6*, 032011.

[5] Yu, J. R.; Gao, G. Y.; Huang, J. R.; Yang, X. X.; Han, J.; Zhang, H.; Chen, Y. H.; Zhao, C. L.; Sun, Q. J.; Wang, Z. L. Contact-electrification-activated artificial afferents at femtojoule energy. *Nat. Commun.* **2021**, *12*, 1581.

[6] Huang, Y.; Zhou, Y. Q.; Wieland, S.; Li, Y. C.; Zhao, N.; Zaumseil, J. Tunable tactile synapses enabled by erasable doping in iongel-gated nanotube network transistors. *Adv. Funct. Mater.*, in press, DOI: 10.1002/adfm.202423030.

[7] Yang, X. X.; Yu, J. R.; Zhao, J.; Chen, Y. H.; Gao, G. Y.; Wang, Y. F.; Sun, Q. J.; Wang, Z. L. Mechanoplastic tribotronic floating-gate neuromorphic transistor. *Adv. Funct. Mater.* **2020**, *30*, 2002506.

[8] Kim, S.; Kwon, O.; Kim, S.; Jang, S.; Yu, S.; Lee, C. H.; Choi, Y. Y.; Cho, S. Y.; Kim, K. C.; Yu, C. J. et al. Modulating synaptic plasticity with metal–organic framework for information-filterable artificial retina. *Nat. Commun.* **2025**, *16*, 162.

[9] Sahoo, S.; Varghese, A.; Sadashiva, A.; Goyal, M.; Sakhuja, J.; Bhowmik, D.; Lodha, S. Vertically integrated dual-memtransistor enabled reconfigurable heterosynaptic sensorimotor networks and in-memory neuromorphic computing. *ACS Nano* **2025**, *19*, 13287–13299.

[10] Kim, J. H.; Sun, Q. J.; Seo, S. Pressure dependent current-controllable devices based on organic thin film transistors by soft-contact lamination. *Org. Electron.* **2010**, *11*, 964–968.

[11] Wang, Y. F.; Sun, Q. J.; Yu, J. R.; Xu, N.; Wei, Y. C.; Cho, J. H.; Wang, Z. L. Boolean logic computing based on neuromorphic transistor. *Adv. Funct. Mater.* **2023**, *33*, 2305791.

[12] Wei, X.; Wu, Z. X.; Gao, H. F.; Cao, S. Q.; Meng, X.; Lan, Y. Q.; Su, H. X.; Qin, Z. L.; Liu, H.; Du, W. X. et al. Mechano-gated iontronic piezomemristor for temporal-tactile neuromorphic plasticity. *Nat. Commun.* **2025**, *16*, 1060.

[13] Serghiou, T.; Fernandes, J. D.; Karthikeyan, V.; Assi, D. S.; Vieira, D. H.; Alves, N.; Kettle, J. Sustainable and tunable synaptic electrolyte-gated organic field-effect transistors (EGOFETs) for light adaptive visual perceptive systems. *Adv. Funct. Mater.* **2025**, *35*, 2417355.

[14] Zhang, Y. C.; Liu, L.; Tu, B.; Cui, B.; Guo, J. H.; Zhao, X.; Wang, J. Y.; Yan, Y. An artificial synapse based on molecular junctions. *Nat. Commun.* **2023**, *14*, 247.

[15] Jo, Y.; Woo, D. Y.; Noh, G.; Park, E.; Kim, M. J.; Sung, Y. W.; Lee, D. K.; Park, J.; Kim, J.; Jeong, Y. et al. Hardware implementation of network connectivity relationships using 2D hBN-based artificial neuron and synaptic devices. *Adv. Funct. Mater.* **2024**, *34*, 2309058.

[16] Li, Y. N.; Zhang, Y.; Wang, Y. Q.; Sun, J. Y.; You, Q.; Zhu, M. Q.; Li, L. N.; Deng, T. Polarization-sensitive optoelectronic synapse based on 3D graphene/MoS_2 heterostructure. *Adv. Funct. Mater.* **2024**, *34*, 2302288.

[17] Kim, S.; Ju, D.; Kim, S. Implementation of artificial synapse using IGZO-based resistive switching device. *Materials* **2024**, *17*, 481.

[18] Jeon, D.; Lee, S. H.; Lee, S. N. Enhanced long-term in-sensing memory in ZnO nanoparticle-based optoelectronic synaptic devices through thermal treatment. *Materials* **2025**, *18*, 1321.

[19] Ju, D.; Kim, S. Versatile NbO_x-based volatile memristor for artificial intelligent applications. *Adv. Funct. Mater.* **2024**, *34*, 2409436.

[20] Pazos, S.; Zhu, K. C.; Villena, M. A.; Alharbi, O.; Zheng, W. W.; Shen, Y. Q.; Yuan, Y.; Ping, Y.; Lanza, M. Synaptic and neural behaviours in a standard silicon transistor. *Nature* **2025**, *640*, 69–76.

[21] Yang, H. S.; Kim, W.; Yoo, H.; Lee, E. K. Organic electrochemical transistors with microporous structures via phase-separation for enhancing long-term plasticity in artificial synapses. *Adv. Mater. Technol.* **2024**, *9*, 2400478.

[22] Song, O.; Cho, Y.; Cho, S. Y.; Kang, J. Solution-processing approach of nanomaterials toward an artificial sensory system. *Int. J. Extrem. Manuf.* **2024**, *6*, 052001.

[23] Sun, B.; Guo, T.; Zhou, G. D.; Ranjan, S.; Jiao, Y. X.; Wei, L.; Zhou, Y. N.; Wu, A. Y. Synaptic devices based neuromorphic computing applications in artificial intelligence. *Mater. Today Phys.* **2021**, *18*, 100393.

[24] Gao, K. K.; Sun, B.; Yang, B.; Cao, Z. L.; Cui, Y.; Wang, M. N.; Kong, C. C.; Zhou, G. D.; Luo, S. H.; Chen, X. L. et al. An organic artificial synaptic memristor for neuromorphic computing. *Appl. Mater. Today* **2025**, *43*, 102628.

[25] Du, J. M.; Sun, B.; Yang, C.; Cao, Z. L.; Zhou, G. D.; Wang, H. Y.; Chen, Y. Z. Ferroelectric memristor and its neuromorphic computing applications. *Mater. Today Phys.* **2025**, *50*, 101607.

[26] Cho, S. W.; Kwon, S. M.; Kim, Y. H.; Park, S. K. Recent progress in transistor-based optoelectronic synapses: From neuromorphic computing to artificial sensory system. *Adv. Intell. Syst.* **2021**, *3*, 2000162.

[27] He, Y. L.; Yang, Y.; Nie, S.; Liu, R.; Wan, Q. Electric-double-layer transistors for synaptic devices and neuromorphic systems. *J. Mater. Chem. C* **2018**, *6*, 5336–5352.

[28] Chen, S. C.; Zhang, T.; Tappertzhofen, S.; Yang, Y. C.; Valov, I. Electrochemical-memristor-based artificial neurons and synapses-fundamentals, applications, and challenges. *Adv. Mater.* **2023**, *35*, 2301924.

[29] Xiong, Y.; Huo, Z. W.; Zhang, J. T.; Liu, Y.; Yue, D. W.; Xu, N.; Gu, R.; Wei, L.; Luo, L.; Chen, M. X. et al. Triboelectric in-sensor deep learning for self-powered gesture recognition toward multifunctional rescue tasks. *Nano Energy* **2024**, *124*, 109465.

[30] Jiao, H. S.; Lin, X. D.; Xiong, Y.; Han, J.; Liu, Y.; Yang, J. H.; Wu, S. S.; Jiang, T.; Wang, Z. L.; Sun, Q. J. Thermal insulating textile based triboelectric nanogenerator for outdoor wearable sensing and interaction. *Nano Energy* **2024**, *120*, 109134.

[31] Xiong, Y.; Luo, L.; Yang, J. H.; Han, J.; Liu, Y.; Jiao, H. S.; Wu, S. S.; Cheng, L. Q.; Feng, Z. Y.; Sun, J. et al. Scalable spinning, winding, and knitting graphene textile TENG for energy harvesting and human motion recognition. *Nano Energy* **2023**, *107*, 108137.

[32] Xiao, Z. H.; Xiao, X. S.; Kong, L. B.; Dong, H. B.; Li, X. Y.; He, B.; Ruan, S. C.; Zhai, J. P.; Zhou, K.; Huang, Q. et al. Preparation of MXene-based hybrids and their application in neuromorphic devices. *Int. J. Extrem. Manuf.* **2024**, *6*, 022006.

[33] Luo, L.; Han, J.; Xiong, Y.; Huo, Z. W.; Dan, X. Z.; Yu, J. R.; Yang,

J. H.; Li, L. L.; Sun, J.; Xie, X. Y. et al. Kirigami interactive triboelectric mechanologic. *Nano Energy* **2022**, *99*, 107345.
[34] Lei, Y. Q.; Yang, J. H.; Xiong, Y.; Wu, S. S.; Guo, W. D.; Liu, G. S.; Sun, Q. J.; Wang, Z. L. Surface engineering AgNW transparent conductive films for triboelectric nanogenerator and self-powered pressure sensor. *Chem. Eng. J.* **2023**, *462*, 142170.
[35] Han, J.; Xu, N.; Yu, J. R.; Wang, Y. F.; Xiong, Y.; Wei, Y. C.; Wang, Z. L.; Sun, Q. J. Energy autonomous paper modules and functional circuits. *Energy Environ. Sci.* **2022**, *15*, 5069–5081.
[36] Gao, Z. Q.; Wu, S. K.; Wei, Y. H.; Ibrahim, M.; Abdelhamid, H. N.; Jiang, G. Y.; Cao, J.; Sun, X. H.; Wen, Z. Holistic and localized preparation methods for triboelectric sensors: Principles, applications and perspectives. *Int. J. Extrem. Manuf.* **2024**, *6*, 052002.
[37] Varshney, U.; Sharma, A.; Singh, P.; Gupta, G. Revealing the photo-sensing capabilities of a super-flexible, paper-based wearable a-Ga_2O_3 self-driven ultra-high-performance solar-blind photodetector. *Chem. Eng. J.* **2024**, *496*, 153910.
[38] Yin, X. M.; Guo, Q. D.; Ji, X. Q.; Li, X. Q.; Xue, H.; Xin, Q.; Zhang, J. W.; Yan, Z. C.; Song, A. M. Paper-based degradable, label-free microRNA sensing platform based on oxide thin-film transistor arrays. *Biosens. Bioelectron.* **2025**, *277*, 117291.
[39] Bushra, K. A.; Prasad, K. S. Paper-based field-effect transistor sensors. *Talanta* **2022**, *239*, 123085.
[40] Li, Z. K.; Yu, A. F.; Zhang, Q.; Zhai, J. Y. Recent advances in fabricating high-performance triboelectric nanogenerators via modulating surface charge density. *Int. J. Extrem. Manuf.* **2024**, *6*, 052003.
[41] Conti, S.; Pimpolari, L.; Calabrese, G.; Worsley, R.; Majee, S.; Polyushkin, D. K.; Paur, M.; Pace, S.; Keum, D. H.; Fabbri, F. et al. Low-voltage 2D materials-based printed field-effect transistors for integrated digital and analog electronics on paper. *Nat. Commun.* **2020**, *11*, 3566.
[42] Grau, G.; Frazier, E. J.; Subramanian, V. Printed unmanned aerial vehicles using paper-based electroactive polymer actuators and organic ion gel transistors. *Microsyst. Nanoeng.* **2016**, *2*, 16032.
[43] Xu, N.; Lin, X. D.; Han, J.; Sun, Q. J. Sustainable paper electronics and neuromorphic paper chip. *Nanotechnology* **2024**, *35*, 222501.
[44] Choi, W.; Shin, J.; Kim, Y. J.; Hur, J.; Jang, B. C.; Yoo, H. Versatile papertronics: Photo-induced synapse and security applications on papers. *Adv. Mater.* **2024**, *36*, 2312831.
[45] Peng, B. Y.; Chan, P. K. L. Flexible organic transistors on standard printing paper and memory properties induced by floated gate electrode. *Org. Electron.* **2014**, *15*, 203–210.
[46] Komatsu, H.; Hosoda, N.; Kounoue, T.; Tokiwa, K.; Ikuno, T. Disposable and flexible paper-based optoelectronic synaptic devices for physical reservoir computing. *Adv. Electron. Mater.* **2024**, *10*, 2300749.
[47] Martins, R.; Gaspar, D.; Mendes, M. J.; Pereira, L.; Martins, J.; Bahubalindruni, P.; Barquinha, P.; Fortunato, E. Papertronics: Multigate paper transistor for multifunction applications. *Appl. Mater. Today* **2018**, *12*, 402–414.
[48] Kanaparthi, S.; Badhulika, S. Solvent-free fabrication of a biodegradable all-carbon paper based field effect transistor for human motion detection through strain sensing. *Green Chem.* **2016**, *18*, 3640–3646.
[49] Wei, Y. C.; Yu, J. R.; Li, Y. H.; Wang, Y. F.; Huo, Z. W.; Cheng, L. Q.; Yue, D. W.; Zhang, K. T.; Gong, J.; Wang, J. et al. Mechano-driven logic-in-memory with neuromorphic triboelectric charge-trapping transistor. *Nano Energy* **2024**, *126*, 109622.
[50] Lin, X. D.; Li, Y. H.; Lei, Y. Q.; Sun, Q. J. Electric-double-layer-gated 2D transistors for bioinspired sensors and neuromorphic devices. *Int. J. Smart Nano Mater.* **2024**, *15*, 238–259.
[51] Niu, S. M.; Liu, Y.; Wang, S. H.; Lin, L.; Zhou, Y. S.; Hu, Y. F.; Wang, Z. L. Theoretical investigation and structural optimization of single-electrode triboelectric nanogenerators. *Adv. Funct. Mater.* **2014**, *24*, 3332–3340.
[52] Niu, S. M.; Wang, S. H.; Lin, L.; Liu, Y.; Zhou, Y. S.; Hu, Y. F.; Wang, Z. L. Theoretical study of contact-mode triboelectric nanogenerators as an effective power source. *Energy Environ. Sci.* **2013**, *6*, 3576–3583.
[53] Niu, S. M.; Zhou, Y. S.; Wang, S. H.; Liu, Y.; Lin, L.; Bando, Y.; Wang, Z. L. Simulation method for optimizing the performance of an integrated triboelectric nanogenerator energy harvesting system. *Nano Energy* **2014**, *8*, 150–156.
[54] Niu, S. M.; Liu, Y.; Wang, S. H.; Lin, L.; Zhou, Y. S.; Hu, Y. F.; Wang, Z. L. Theory of sliding-mode triboelectric nanogenerators. *Adv. Mater.* **2013**, *25*, 6184–6193.
[55] Zhang, H.; Zhang, C. H.; Zhang, J. W.; Quan, L. W.; Huang, H. Y.; Jiang, J. Q.; Dong, S. R.; Luo, J. K. A theoretical approach for optimizing sliding-mode triboelectric nanogenerator based on multi-parameter analysis. *Nano Energy* **2019**, *61*, 442–453.
[56] Chu, Y.; Han, R. X.; Meng, F. Y.; Cao, Z. Y.; Wang, S. W.; Dong, K. K.; Yang, S. S.; Liu, H. L.; Ye, X. Y.; Tang, F. Theoretical study on the output of contact–separation triboelectric nanogenerators with arbitrary charging and grounding conditions. *Nano Energy* **2021**, *89*, 106383.
[57] Zhang, H.; Quan, L. W.; Chen, J. K.; Xu, C. K.; Zhang, C. H.; Dong, S. R.; Lü, C. F.; Luo, J. K. A general optimization approach for contact–separation triboelectric nanogenerator. *Nano Energy* **2019**, *56*, 700–707.
[58] Yang, B.; Zeng, W.; Peng, Z. H.; Liu, S. R.; Chen, K.; Tao, X. M. A fully verified theoretical analysis of contact-mode triboelectric nanogenerators as a wearable power source. *Adv. Energy Mater.* **2016**, *6*, 1600505.
[59] Wu, C. X.; Kim, T. W.; Park, J. H.; Koo, B.; Sung, S.; Shao, J. J.; Zhang, C.; Wang, Z. L. Self-powered tactile sensor with learning and memory. *ACS Nano* **2020**, *14*, 1390–1398.
[60] Yu, J. R.; Yang, X. X.; Gao, G. Y.; Xiong, Y.; Wang, Y. F.; Han, J.; Chen, Y. H.; Zhang, H.; Sun, Q. J.; Wang, Z. L. Bioinspired mechano-photonic artificial synapse based on graphene/MoS_2 heterostructure. *Sci. Adv.* **2021**, *7*, eabd9117.
[61] Chen, L. B.; Wen, C. Y.; Zhang, S. L.; Wang, Z. L.; Zhang, Z. B. Artificial tactile peripheral nervous system supported by self-powered transducers. *Nano Energy* **2021**, *82*, 105680.
[62] Bao, C.; Seol, S. K.; Kim, W. S. A 3D integrated neuromorphic chemical sensing system. *Sens. Actuators B: Chem.* **2021**, *332*, 129527.
[63] Liao, X. Q.; Song, W. T.; Zhang, X. Y.; Yan, C. Q.; Li, T. L.; Ren, H. L.; Liu, C. Z.; Wang, Y. T.; Zheng, Y. J. A bioinspired analogous nerve towards artificial intelligence. *Nat. Commun.* **2020**, *11*, 268.
[64] Zhang, C.; Zhang, L. M.; Tang, W.; Han, C. B.; Wang, Z. L. Tribotronic logic circuits and basic operations. *Adv. Mater.* **2015**, *27*, 3533–3540.
[65] Ma, M. X.; Ni, Y.; Chi, Z. R.; Meng, W. Q.; Yu, H. Y.; Gong, J. D.; Wei, H. H.; Han, H.; Wang, X. R.; Xu, W. T. Multiplexed neurochemical transmission emulated using a dual-excitatory synaptic transistor. *npj 2D Mater. Appl.* **2021**, *5*, 23.
[66] He, Z. Y.; Wang, T. Y.; Meng, J. L.; Zhu, H.; Ji, L.; Sun, Q. Q.; Chen, L.; Zhang, D. W. CMOS back-end compatible memristors for *in situ* digital and neuromorphic computing applications. *Mater. Horiz.* **2021**, *8*, 3345–3355.
[67] Xu, X. J.; Zhou, X. F.; Wang, T. Y.; Shi, X.; Liu, Y.; Zuo, Y.; Xu, L. M.; Wang, M. Y.; Hu, X. F.; Yang, X. J. et al. Robust DNA-bridged memristor for textile chips. *Angew. Chem., Int. Ed.* **2020**, *59*, 12762–12768.
[68] Lin, P.; Li, C.; Wang, Z. R.; Li, Y. N.; Jiang, H.; Song, W. H.; Rao, M. Y.; Zhuo, Y.; Upadhyay, N. K.; Barnell, M. et al. Three-dimensional memristor circuits as complex neural networks. *Nat. Electron.* **2020**, *3*, 225–232.
[69] Wang, T. Y.; Meng, J. L.; Rao, M. Y.; He, Z. Y.; Chen, L.; Zhu, H.; Sun, Q. Q.; Ding, S. J.; Bao, W. Z.; Zhou, P. et al. Three-dimensional nanoscale flexible memristor networks with ultralow power for information transmission and processing application. *Nano Lett.* **2020**, *20*, 4111–4120.
[70] Wang, T. Y.; Meng, J. L.; Chen, L.; Zhu, H.; Sun, Q. Q.; Ding, S. J.; Bao, W. Z.; Zhang, D. W. Flexible 3D memristor array for binary

storage and multi-states neuromorphic computing applications. *InfoMat* **2021**, *3*, 212–221.
[71] Liu, G. C.; Li, Q. Y.; Shi, W.; Liu, Y. W.; Liu, K.; Yang, X. L.; Shao, M. C.; Guo, A. K.; Huang, X.; Zhang, F. et al. Ultralow-power and multisensory artificial synapse based on electrolyte-gated vertical organic transistors. *Adv. Funct. Mater.* **2022**, *32*, 2200959.
[72] Kapur, O.; Guo, D. K.; Reynolds, J.; Han, Y. S.; Beanland, R.; Jiang, L. D. ; de Groot, C. H.; Huang, R. M. Back-end-of-line SiC-based memristor for resistive memory and artificial synapse. *Adv. Electron. Mater.* **2022**, *8*, 2200312.
[73] Zhang, S.; Yang, L.; Jiang, C. P.; Sun, L. X.; Guo, K. X.; Han, H.; Xu, W. T. Digitally aligned ZnO nanowire array based synaptic transistors with intrinsically controlled plasticity for short-term computation and long-term memory. *Nanoscale* **2021**, *13*, 19190–19199.
[74] Ni, Y.; Feng, J. L.; Liu, J. Q.; Yu, H.; Wei, H. H.; Du, Y.; Liu, L.; Sun, L.; Zhou, J. L.; Xu, W. T. An artificial nerve capable of UV-perception, NIR–vis switchable plasticity modulation, and motion state monitoring. *Adv. Sci.* **2022**, *9*, 2102036.
[75] Pyo, S.; Lee, J.; Kim, W.; Jo, E.; Kim, J. Multi-layered, hierarchical fabric-based tactile sensors with high sensitivity and linearity in ultrawide pressure range. *Adv. Funct. Mater.* **2019**, *29*, 1902484.
[76] Liu, Y. Q.; Zhong, J. F.; Li, E. L.; Yang, H. H.; Wang, X. M.; Lai, D. X.; Chen, H. P.; Guo, T. L. Self-powered artificial synapses actuated by triboelectric nanogenerator. *Nano Energy* **2019**, *60*, 377–384.
[77] Zeng, J. H.; Zhao, J. Q.; Bu, T. Z.; Liu, G. X.; Qi, Y. C.; Zhou, H.; Dong, S. C.; Zhang, C. A flexible tribotronic artificial synapse with bioinspired neurosensory behavior. *Nano-Micro Lett.* **2023**, *15*, 18.
[78] Zhang, S.; Guo, J. M.; Liu, L. L.; Ruan, H. R.; Kong, C. Y.; Yuan, X. B.; Zhang, B.; Gu, G. Q.; Cui, P.; Cheng, G. et al. The self-powered artificial synapse mechanotactile sensing system by integrating triboelectric plasma and gas-ionic-gated graphene transistor. *Nano Energy* **2022**, *91*, 106660.
[79] Lee, Y. R.; Trung, T. Q.; Hwang, B. U.; Lee, N. E. A flexible artificial intrinsic-synaptic tactile sensory organ. *Nat. Commun.* **2020**, *11*, 2753.
[80] Feng, Z. Y.; Yu, J. R.; Wei, Y. C.; Wang, Y. F.; Tian, B. B.; Li, Y. H.; Cheng, L. Q.; Wang, Z. L.; Sun, Q. J. Tribo-ferro-optoelectronic neuromorphic transistor of α-In_2Se_3. *Brain-X* **2023**, *1*, e24.
[81] Gao, C. F.; Nie, Q. F.; Lin, C. Y.; Huang, F. M.; Wang, L. J.; Xia, W.; Wang, X.; Hu, Z. G.; Li, M. J.; Lu, H. W. et al. Touch-modulated van der Waals heterostructure with self-writing power switch for synaptic simulation. *Nano Energy* **2022**, *91*, 106659.

Nuo Xu received her B.S. degree from South China University in 2017. She is now a PhD student in the School of Physical Science and Engineering Technology, Guangxi University, where she is co-trained at the Institute of Nanoenergy and Nanosystems, Beijing, under the supervision of Prof. Qijun Sun. Her research focuses on the study of flexible electronic circuits and neuromorphic devices.

Zhong Lin Wang received his Ph.D in physics from Arizona State University. He is now the Hightower Chair in Materials Science and Engineering, Regents' Professor, Engineering Distinguished Professor and Director, Center for Nanostructure Characterization, at Georgia Tech. Dr. Wang has made original and innovative contributions to the synthesis, discovery, characterization and understanding of fundamental physical properties of oxide nanobelts and nanowires, as well as applications of nanowires in energy sciences, electronics, optoelectronics and biological science. He pioneered the field of piezotronics and piezo-phototronics by introducing piezoelectric potential gated charge transport process in fabricating new electronic and optoelectronic devices.

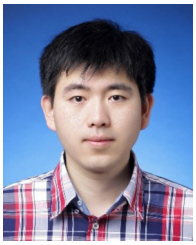

Qijun Sun has joined Beijing Institute of Nanoenergy and Nanosystems, Chinese Academy of Sciences (BINN, CAS) since 2016, as the principal investigator of Functional Soft Electronics Lab. The main research interests of his group include triboiontronic devices, mechanoplastic neuromorphic transistors, artificial synaptic devices, electronic skin, two-dimensional (2D) materials based flexible semiconductor devices, human-machine interactive systems and micro-nano fabrication, aiming to develop advanced systems for human health monitoring and human-robotic interface.